Aalborg Universitet

AALBORG UNIVERSITY

CFD Simulations of Box Elements

Eldrup, Mads Røge

Publication date:
2026

Document Version
Publisher's PDF, also known as Version of record

Link to publication from Aalborg University

Citation for published version (APA):
Eldrup, M. R. (2026). *CFD Simulations of Box Elements*. Institut for Byggeri, By og Miljø (BUILD), Aalborg Universitet. DCE Technical Reports No. 331

General rights
Copyright and moral rights for the publications made accessible in the public portal are retained by the authors and/or other copyright owners and it is a condition of accessing publications that users recognise and abide by the legal requirements associated with these rights.

- Users may download and print one copy of any publication from the public portal for the purpose of private study or research.
- You may not further distribute the material or use it for any profit-making activity or commercial gain
- You may freely distribute the URL identifying the publication in the public portal -

Take down policy
If you believe that this document breaches copyright please contact us at vbn@aub.aau.dk providing details, and we will remove access to the work immediately and investigate your claim.

Downloaded from vbn.aau.dk on: May 23, 2026

DEPARTMENT OF THE BUILT ENVIRONMENT
AALBORG UNIVERSITY

CFD Simulations of Box Elements

Mads Røge Eldrup

ISSN 1901-726X

DCE Technical Report No. 331

Aalborg University

Department of the Built Environment

Ocean and Coastal Engineering Research Group

DCE Technical Report No. 331

CFD Simulations of Box Elements

by

Mads Røge Eldrup

Published January 2026 by

Aalborg University

Department of the Built Environment

Thomas Manns Vej 23

DK-9220 Aalborg E, Denmark

Printed in Aalborg at Aalborg University

ISSN 1901-726X

DCE Technical Report No. 331

Contents

1. Introduction

This report is part of the EUDP-funded project HydroFlex with project number 640232-511381[1]. The purpose of the report is to evaluate selected capabilities of the commercial Computational Fluid Dynamics (CFD) software STAR-CCM+ by Siemens, specifically for estimating drag coefficients of simple shapes and geometries.

The simulations firstly use simple geometries like squares and rectangles before using the *WindFlex* platform as a reference for the geometries, as illustrated in Figure 1. Additional details about the *WindFlex* model can be found in HydroFlex (2025a).

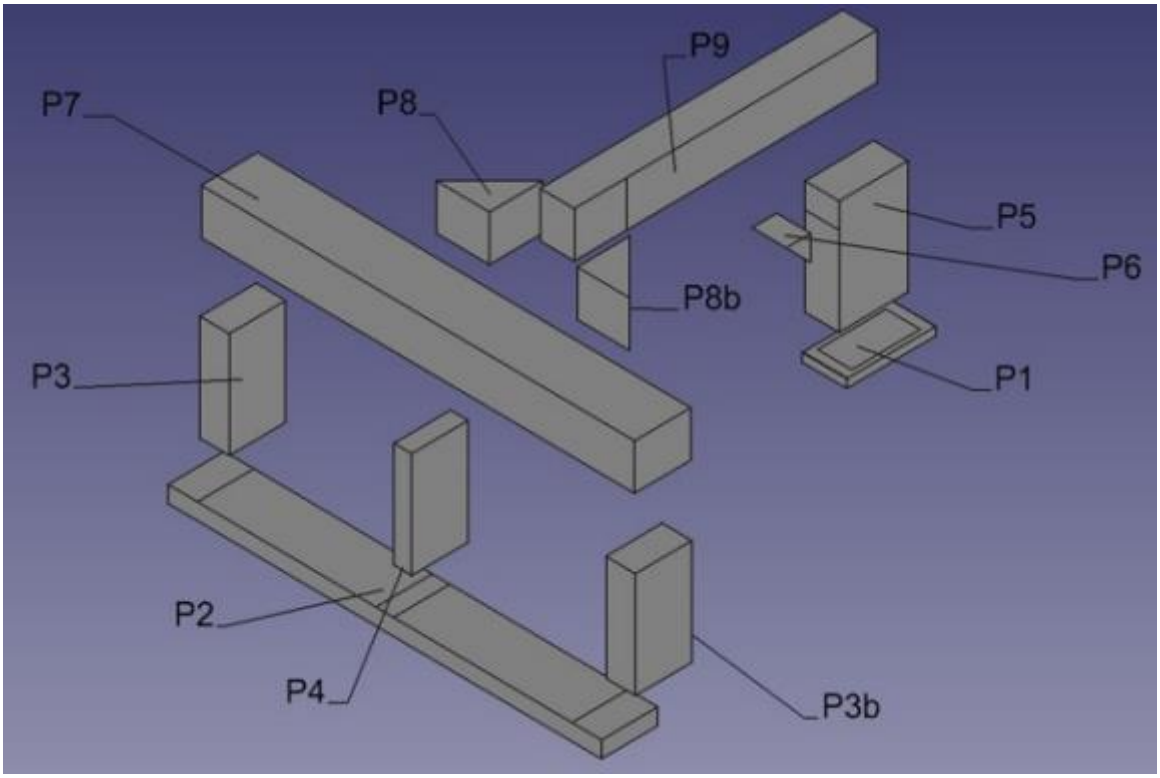

Fig. 1. WindFlex platform and its parts.

The purpose of this report is to gain familiarity with the software by running simple simulations from which drag coefficients are extracted and compared against values reported in the literature. It is not intended to provide an in-depth optimisation of the simulation setup to match these values. Such work will be carried out in a future study that involves direct comparisons between numerical model results and experimental measurements of forced motion on individual platform components. Further details on these experimental tests can be found in HydroFlex (2025b) and (2025c).

A more comprehensive analysis of the entire platform has already been conducted using the open-source CFD model OpenFOAM, as reported by Eskilsson and Kramer (2025).

[1] https://eudp.dk/en/node/16955

1.1. PRESENT WORK

The work presented here represents a self-contained workflow within HydroFlex. It begins with single-phase simulations of simple two-dimensional shapes, such as a square and a rectangle, corresponding to the P5 section of the *WindFlex* platform. The P5 is then gradually extended into a three-dimensional single-phase simulation, culminating in a full three-dimensional two-phase simulation. These results provide the foundation for the next phase of the project, which will involve simulations with moving structures.

It should be noted that the results presented here stem from an initial exploration of STAR-CCM+, serving both as a learning exercise and an evaluation of the software's capabilities. To support the modelling process, tutorials and reference materials were consulted, including selected YouTube videos:

- https://www.youtube.com/watch?v=BZQ8vOz8BtU
- https://www.youtube.com/watch?v=1bXnmyEbinQ
- https://www.youtube.com/watch?v=AZkuHDzSqks&t=2119s

2.STAR CCM+

Simcenter STAR-CCM+ is a commercial multiphysics Computational Fluid Dynamics (CFD) software package developed by Siemens Digital Industries Software (formerly CD-Adapco). It can be used to simulate and analyse fluid flow, heat transfer, and other coupled physical phenomena in real-world conditions.

Key Capabilities:

- **Multiphysics simulation**: fluid flow (single-phase, multiphase), reactive flows, turbulence (RANS, LES, etc.), heat transfer, electromagnetics, fluids-structure interaction, particle dynamics, etc.
- **Meshing & geometry handling**: automatic meshing, support for complex geometries, mesh refinement, thin structures handling, surface remeshing, etc.
- **Design exploration & optimization**: allows users to run many design variations, parametric studies, optimization workflows embedded in the software interface.
- **Workflow automation**: pre-processing, solver setup, post-processing are integrated; users can automate tasks to reduce manual work.
- **Visualization & reporting**: graphical results, animations, photorealistic rendering.

In this report, the tool is used to simulate single-phase and multi-phase flow around simple geometries and to evaluate the resulting forces, which are then compared with values reported in the literature. Figure 2 provides an overview of the STAR-CCM+ interface and the workspace where the model setup is configured.

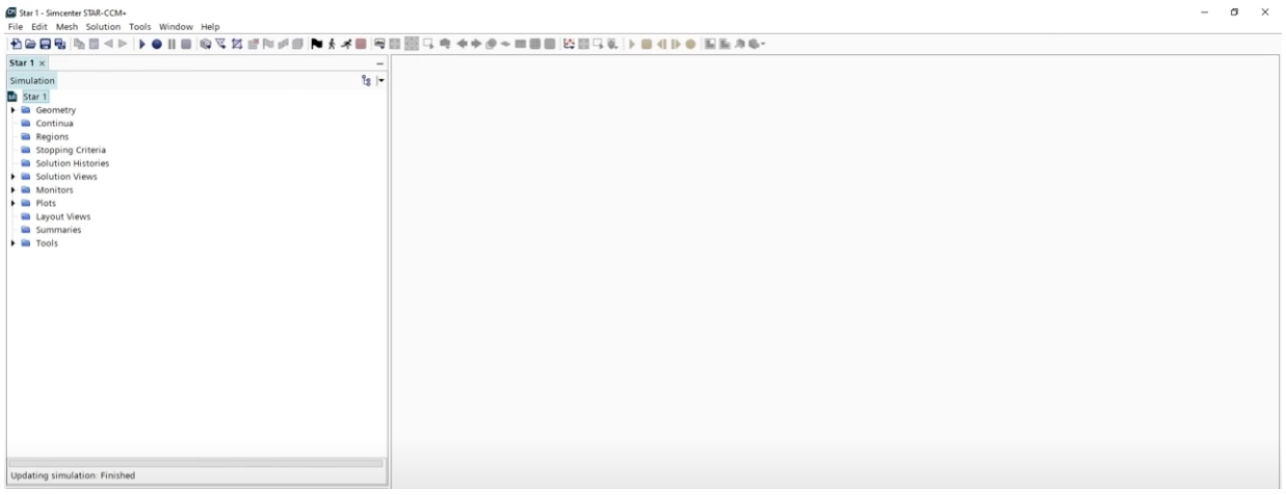

Fig. 2. Workspace for STAR-CCM+.

3. Force Description

To describe the simulated cases, the flow direction, object size, and orientation of the forces can be generalised from the definitions provided in Figure. 3.

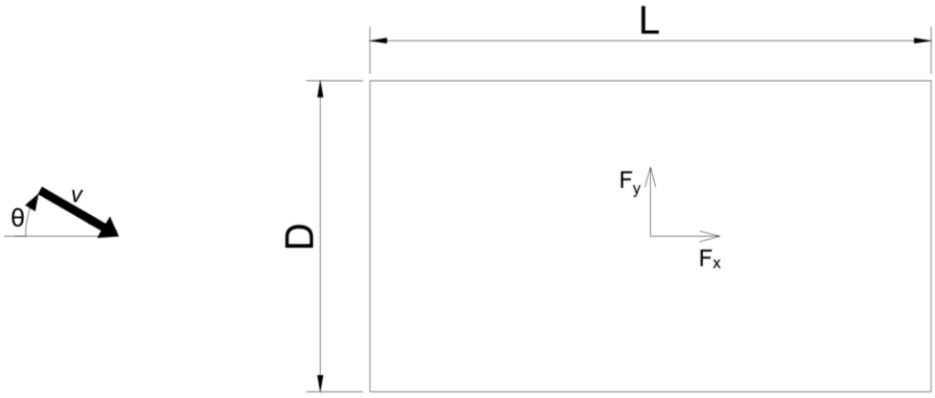

Fig. 3. Parameters used to describe the flow direction, object size, and forces.

In the figure, *v* denotes the flow velocity, while θ represents the angle between the flow direction and the object. By convention, θ = 0 corresponds to flow aligned with the x-axis, and positive values of θ are measured counterclockwise. The dimension *D* refers to the extent in the y-direction, and *L* to the extent in the x-direction. The force components are denoted as F_x in the x-direction and F_y in the y-direction.

The drag coefficient is calculated as the ratio between the force acting on an object and its size, as shown in Equation (1).

$$C_D = \frac{2F_x}{\rho v^2 A} \tag{1}$$

The area is denoted by *A* and represents the cross-sectional area "seen" by the flow. Depending on the chosen definition, this area may vary with the flow direction. However, the references used in this report assume a constant value, independent of flow angle. Accordingly, *A* is taken as the area corresponding to θ = 0, even when the actual flow direction deviates from this angle. For the two-dimensional case shown in Figure 3, the area reduces to *D*. ρ is the density of the water, which in the present case is taken as 998.2 kg/m³, as this is the value from the physical experiments performed at Aalborg University, see HydroFlex (2025a).

The drag coefficient depends on the flow regime, typically described by the Reynolds number *Re*. This number indicates the flow separation, which can be laminar, turbulent, or transient. The *Re* number is given in Equation (2).

$$Re = \frac{\rho v D}{\mu} \tag{2}$$

where μ denotes the dynamic viscosity of the fluid, taken here as 1 mPa·s.

4. Single-Phase Simulation with a Square

4.1. Two-dimensional simulations on Square

Flow around a two-dimensional square is simulated in STAR-CCM+, and the resulting force data are used to calculate the drag coefficient. Since the square has been extensively studied in the literature, reference drag coefficient values are available for comparison with the results obtained from numerical simulations.

4.1.1. Drag coefficient from literature

According to the recommended practice in RP-C205 by DNV (2025), the drag coefficient C_D is a maximum of 2.2 when the flow is perpendicular to one face, and it decreases to 1.3 when the flow direction is rotated by $\theta = 15°$. This was reported for a Reynolds number of 4.7×10^4. The influence of the flow direction on the drag coefficient given by DNV is given in Table 1.

Table 1. Drag coefficient on an inclined square. Taken from Table C-1 in DNV RP-C205 (2025).

θ	0	5	10	15	20	25	30	35	40	45
C_D	2.2	2.1	1.8	1.3	1.9	2.1	2.2	2.3	2.4	2.4

Yen and Yang (2011) tested the drag coefficient on a square experimentally in a two-dimensional setup at Reynolds numbers ranging from 0.6×10^4 to 3.6×10^4. They found the same flow-direction influence as in DNV, but also noted a small effect of Reynolds number, with drag coefficients increasing with Reynolds number. Their results indicate slightly lower drag coefficients than those reported by DNV, which is expected given the higher Reynolds number used in the DNV table. The results from Yen and Yang (2011) are given in Figure 4.

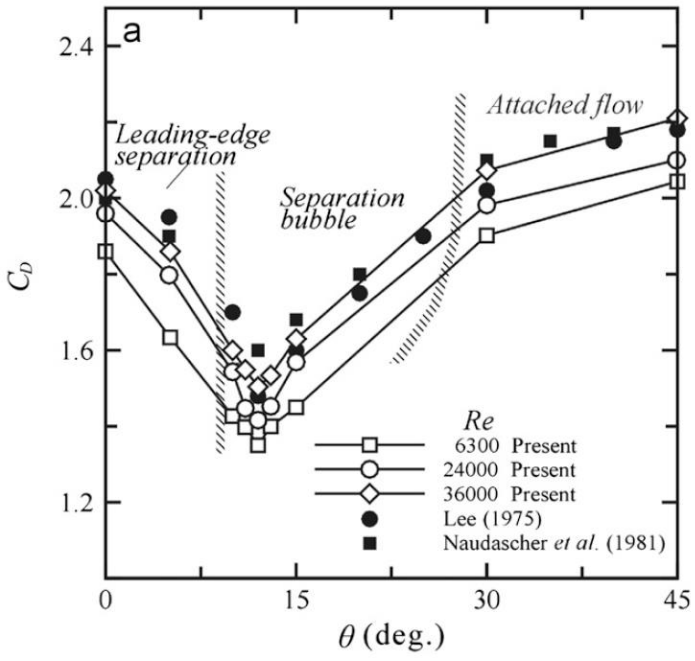

Fig. 4. Drag coefficient on a square. Adopted from Yen and Yang (2011).

4.1.2. Model Set-up

The model set-up used for validation is shown in Figure 5. The model is a 1 × 1 m square with a domain size of 14 m × 19 m. The flow is going from left to right, and the square is placed at a distance of 4 m from the inlet. The simulations are performed with a single phase (water).

The mesh is defined relative to a base element size of 2 mm. Good practice is to perform a mesh-size convergence study, but this has not been done for the given setup, so the value was chosen at random. Generally, it is good practice to refine the mesh at sharp edges and near objects to resolve large flow gradients, boundary-layer effects, and flow separation. Near the square, the mesh consists of 30 prism elements, each 200% the size of the base element. Further away, the mesh is composed of polygonal elements with a *Surface Growth Rate* of 1.025, so the elements increase in size farther from the square. The target mesh size along the domain boundary is set to 1 m, as smaller flow gradients are expected farther from the square. *Wake Refinement* has been applied to mitigate turbulence on the model's lee side. Here, a distance of 4 m behind the square is used with a specified cell size given as 800% of the base element size.

Simulation runs were completed using a steady-state and a transient solver. The steady-state solution is a faster method because it assumes constant flow conditions and is thus independent of time. However, due to the expected flow separation behind the square at higher Reynolds numbers, this assumption is not accurate. The transient simulation is more computationally demanding but captures time-dependent effects such as flow separation. For the transient simulation, the time step is controlled by the Courant-Friedrichs-Lewy (CFL) number. The used CFL is set to 0.5 and should usually be below 1. However, because the CFL number may exceed the target value, it is often recommended to use a smaller value as a precaution.

Turbulence modelling is required to provide an approximate representation of the effects of turbulent eddies on the mean flow, enabling realistic predictions of forces, pressure distributions, and flow separation. In this work, a k–ε turbulence model has been selected because it is robust, widely used, and computationally efficient for general-purpose simulations. However, alternative models such as k–ω SST may provide more accurate results for the given conditions

The left, top and bottom boundaries in Figure 5 is given as a velocity inlet with a constant velocity. Alternatively, the top and bottom boundaries could have been specified as symmetry planes, but the influence of this has not been tested. The right boundary is a pressure outlet where pressure is set to 0 Pa. The boundary of the square is set to a wall.

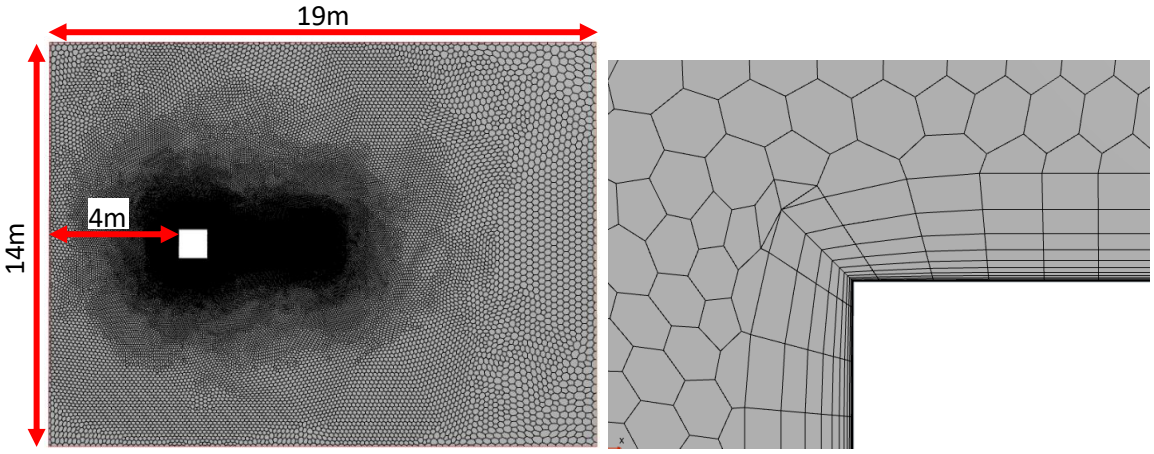

Fig. 5. The left shows the entire model domain. The right shows a close-up of the corner of the object.

4.1.3. RESULTS

The Reynolds numbers tested by Yen and Yang (2011) are reproduced in the current setup for direct comparison. To get the same Reynolds numbers, the two different flow velocities given in Table 2 are applied.

Table 2. Reynolds number and corresponding flow speed.

Re	v [m/s]
0.6×10^4	0.0063
3.6×10^4	0.0360

Figure 6 shows the drag coefficient from the steady-state simulation with the low Reynolds number. In these simulations, the effect of under-relaxation was also investigated. Under-relaxation controls the allowed change in pressure and velocity during each iteration. Lower values generally yield a more stable solution but require more iterations to converge. The standard under-relaxation factors for velocity and pressure are 0.7 and 0.3, respectively.

To assess their influence, both values were reduced to 0.1 in the results shown at the bottom of Figure 6. The results indicate that more iterations are needed for the drag coefficient to converge with lower under-relaxation factors. It is also observed that the fluctuations of the drag coefficient are slower with the reduced under-relaxation. Additionally, the drag coefficient is slightly reduced in the simulations with lower under-relaxation, as shown in Table 3.

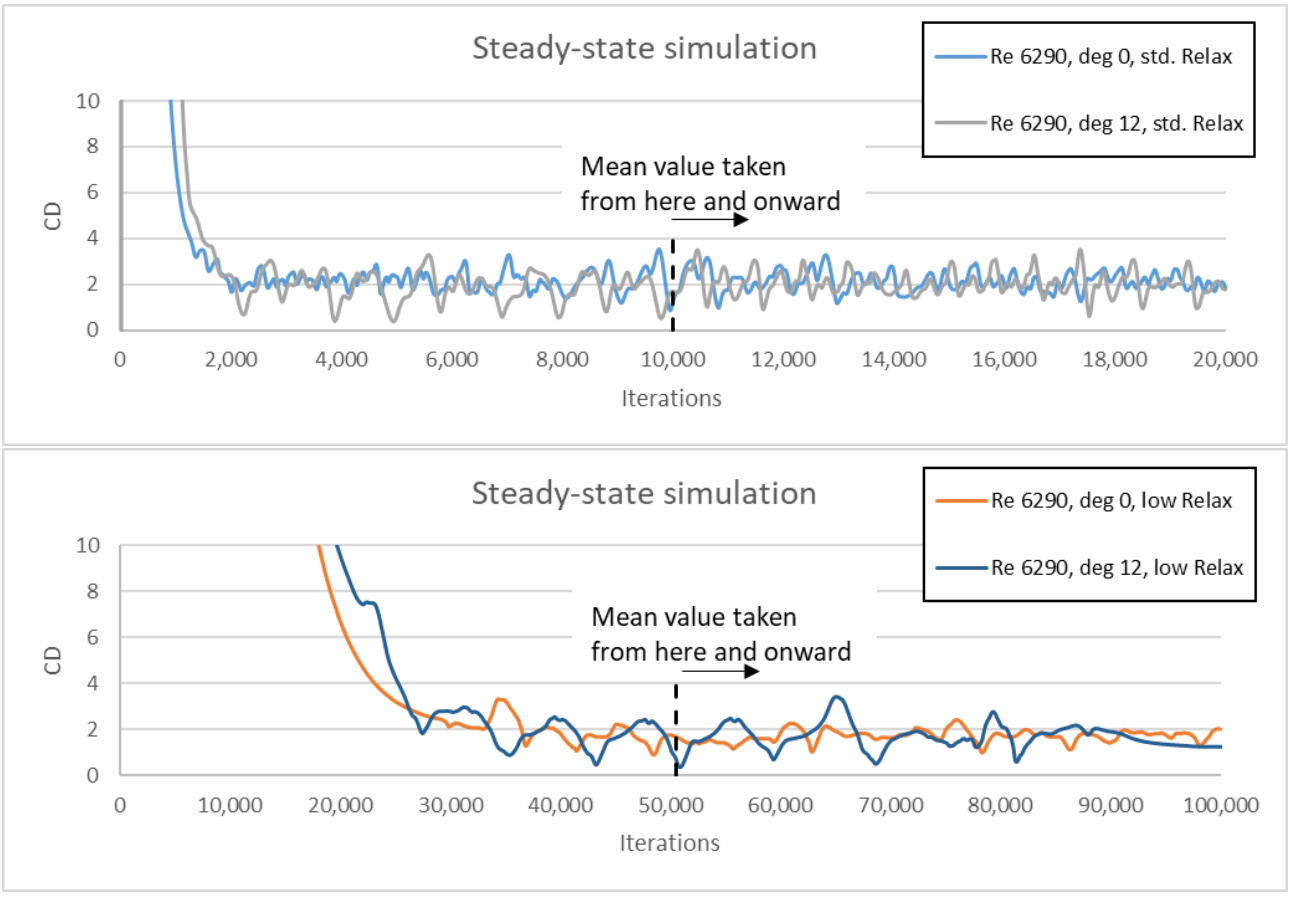

Fig. 6. Drag coefficient for steady-state solution and the influence of under-relaxation for low Reynolds number.

Figure 7 shows the same as Figure 6 but for the high Reynolds simulations. For the standard values of the relaxation, larger oscillations are observed when the Reynolds number is increased. This is less visible for low relaxation values, which “dampens” the solution.

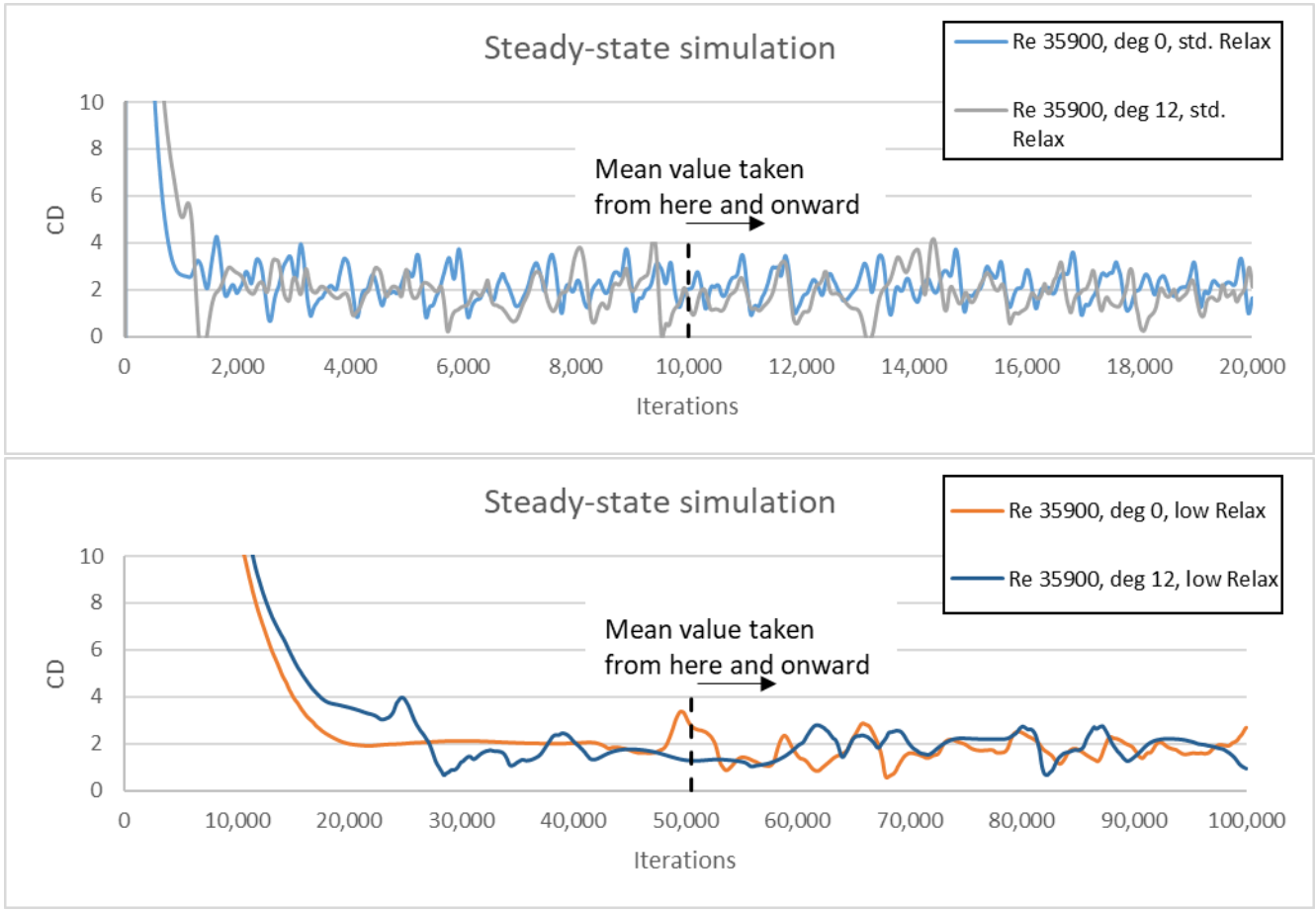

Fig. 7. Drag coefficient for steady-state solution and the influence of under-relaxation for high Reynolds number.

Figure 8 shows the simulated drag coefficient from the transient solver. Instead of the number of iterations, a time-dependent solution is now provided. A repeatable pattern is observed for θ = 12, while the solution with θ = 0 is not repeating, but the reason for this is not studied further. It is also observed that larger variations in the drag coefficient are obtained for the rotated flow.

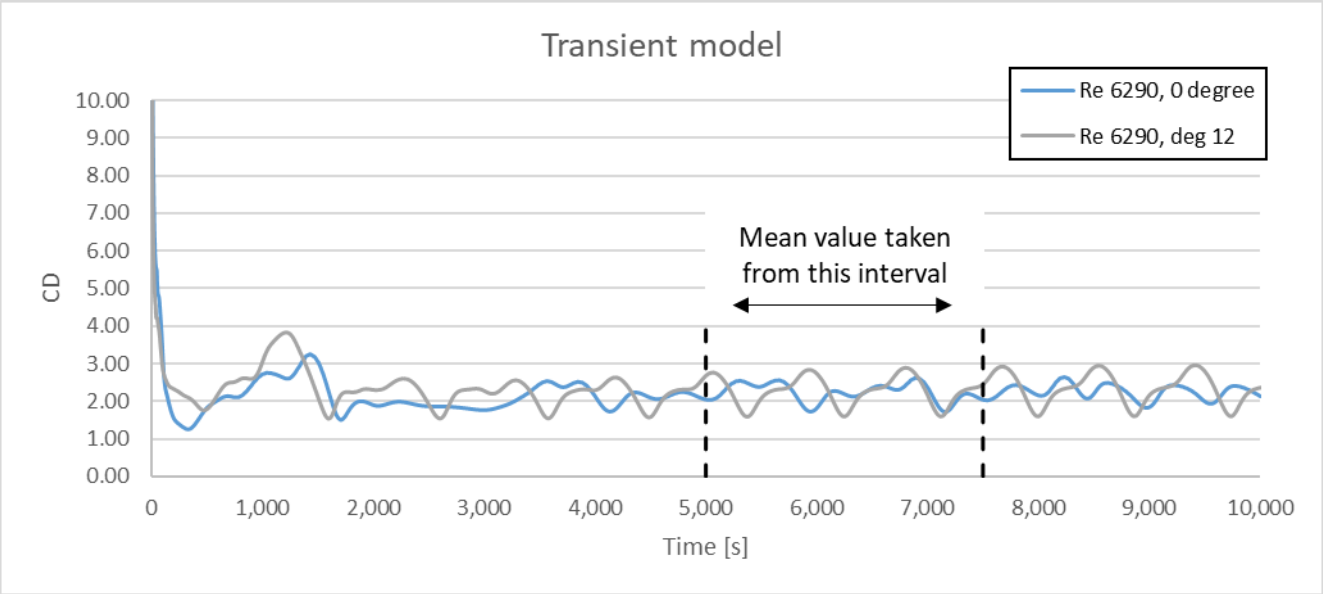

Fig. 8. Drag coefficient for the transient solution for low Reynolds number.

Figure 9 presents the results for the simulations with the higher Reynolds number. In this case, the flow is significantly faster, which is also reflected in the more rapid oscillations compared with Figure 8. It can further be observed that both flow directions have reached a stable, repeating pattern. Moreover, the case with θ = 12 exhibits a smaller variation, while the case with θ = 0 shows a slight increase in variation.

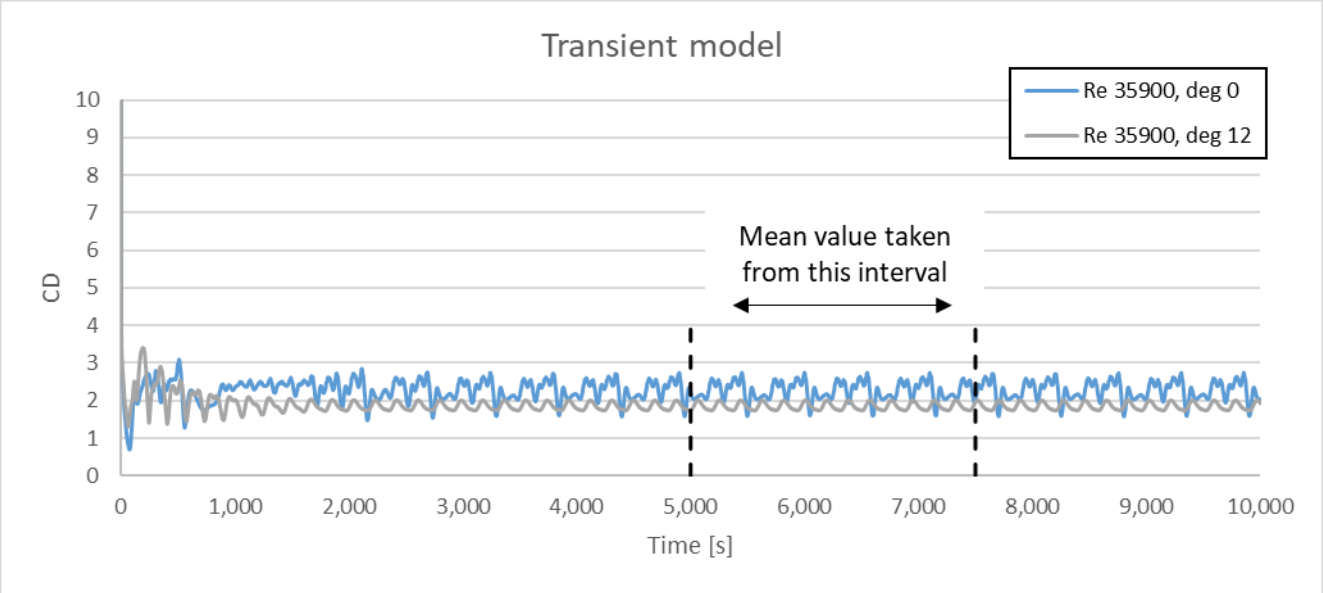

Fig. 9. Drag coefficient for the transient solution for high Reynolds number.

Table 3 presents the results for the different solution methods, Reynolds numbers, and flow orientations. It is observed that the steady-state solution with reduced relaxation values yields a lower drag coefficient than when using the standard values. The steady-state solution with standard relaxation values and the transient simulation show similar drag coefficients. The flow direction has little influence on the average drag at low Reynolds numbers, but the effect becomes more pronounced at higher Reynolds numbers. The underlying cause of this increased sensitivity at high Reynolds numbers has not been further investigated.

Table 3. Drag coefficients for steady-state and transient simulations.

Re	Orientation [deg]	Model	CD
0.6×10^4	0	Steady-state (std.)	2.12
		Steady-state (low)	1.74
		Transient	2.23
	12	Steady-state (std.)	2.04
		Steady-state (low)	1.77
		Transient	2.30
3.6×10^4	0	Steady-state (std.)	2.18
		Steady-state (low)	1.80
		Transient	2.25
	12	Steady-state (std.)	1.82
		Steady-state (low)	1.78
		Transient	1.86

4.1.4. Discussion

Figure 10 compares the drag coefficients from the present simulations with values reported by DNV and by Yen and Yang (2011). In the low-Reynolds-number simulations, only minor dependence on flow direction was observed, contrary to what is reported in the literature. This suggests that additional investigation is needed when simulations must be performed at low Reynolds numbers.

At high Reynolds numbers, a general decrease in drag coefficient is observed, except for the steady-state solution with low relaxation values. The steady-state simulation with standard relaxation parameters and the transient simulation both agree well with the reference data for θ = 0°. For θ = 12°, they deviate more, but still correctly reproduce the expected reduction in drag coefficient.

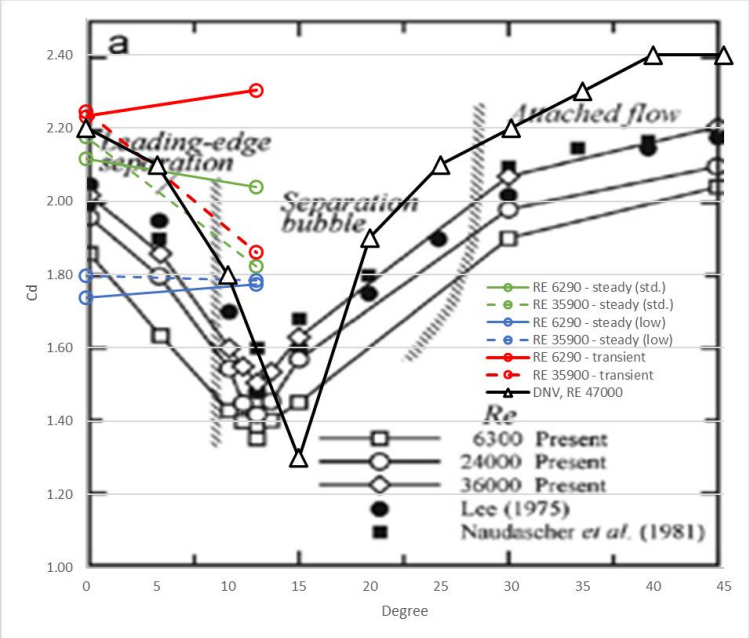

Fig. 10. Drag coefficients from Yen and Yang (2011), DNV and present simulations.

5. Single-Phase Simulation with a Rectangular Box

5.1. Two-dimensional simulation on rectangular box

The flow around a two-dimensional rectangle, with dimensions corresponding to the experimentally tested P5 leg, is simulated in STAR-CCM+. The resulting force data are then used to compute the drag coefficient. Drag-coefficient values for rectangular bodies are available in the literature and thus provide a basis for comparing and validating numerical results.

5.1.1. Drag coefficient from literature

Simulations are carried out on a two-dimensional representation of the P5 leg of the WindFlex model, which has a rectangular shape, see Figure 11.

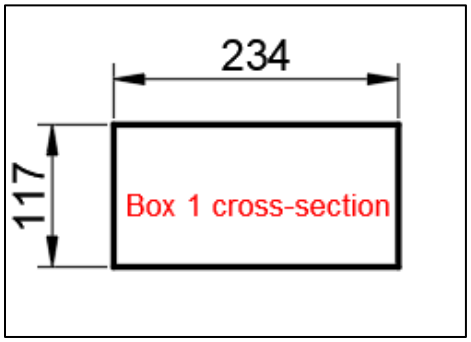

Fig. 11. Top-view cross-sectional dimensions of the P5 leg, as tested experimentally in HydroFlex (2025b).

Figure 12 shows the drag coefficient for a rectangular shape as a function of side-length ratio, based on Blevins (1984). Based on Figure 11 with flow coming from left to right this gives the side-length ratio 234/117 = 2 with a C_D = 1.6.

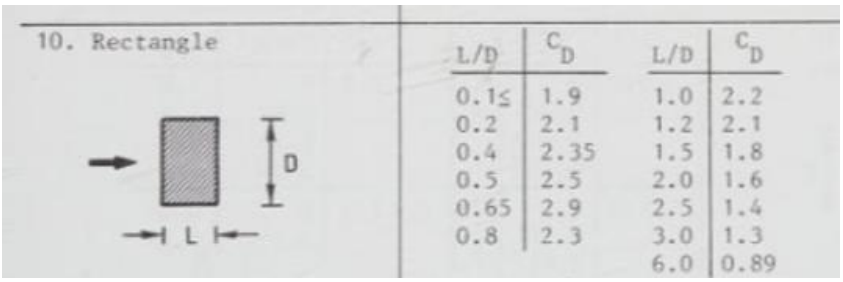
10. Rectangle

L/D	C_D	L/D	C_D
0.1≤	1.9	1.0	2.2
0.2	2.1	1.2	2.1
0.4	2.35	1.5	1.8
0.5	2.5	2.0	1.6
0.65	2.9	2.5	1.4
0.8	2.3	3.0	1.3
		6.0	0.89

Fig. 12. Drag coefficient on a rectangular shape, depending on the side length ratio, taken from Blevins (1984).

5.1.2. Set-up of simulation in STAR-CCM+

Figure 13 shows the computational domain used for the two-dimensional simulations of the P5 leg. The domain extends 14 times the model width and 16.7 times its length. These values were chosen arbitrarily,

and no assessment has been performed to determine potential boundary effects or whether a larger domain would be necessary.

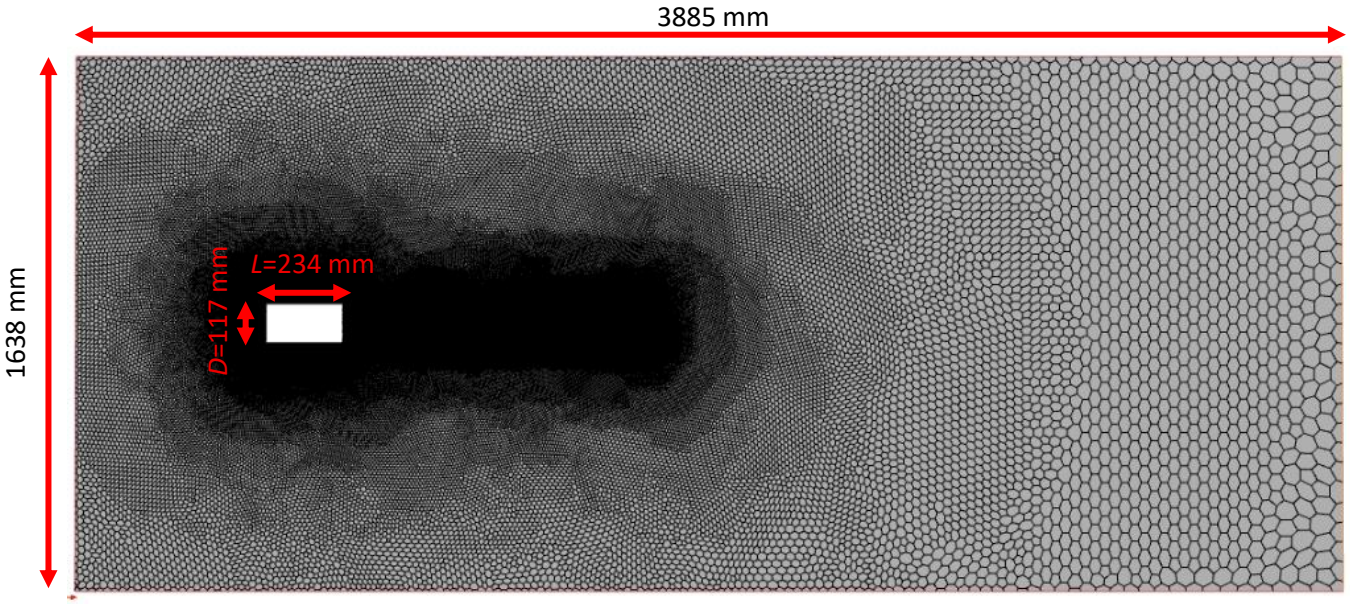

Fig. 13. Model domain in STAR-CCM+ for a rectangular object.

For future work, the intention is to apply a forced sinusoidal motion to the P5 leg or other components. In such cases, steady-state models are not applicable because time dependence is essential. Therefore, the simulations are carried out only with the transient model described earlier.

5.1.3. RESULTS

A convergence analysis is conducted for the current setup to ensure the accuracy and stability of the numerical simulations. In this analysis, the base size of the elements is changed while the remaining relative size with respect to the base size is kept constant, as given in section 4.1.2. The velocity of the flow is set to 0.0707 m/s, a value also used in the physical testing campaign in HydroFlex (2025b), giving Re = 8.26 X 10^3 according to Eq. (2). The results are seen in Table 4. The table displays the base cell size and the total number of cells in the simulation. The y^+ parameter characterises the near-wall mesh resolution and assesses how accurately the boundary layer is resolved. In STAR-CCM+, the near-wall flow is modelled using wall functions that switch between two formulations based on the value of y+. A rule of thumb is that y+ should be either below 5 (viscous sublayer) or above 20-30 (Logarithmic layer) when using the “All y+” approach, which uses or blends the “high y+” and “low y+” wall-function models depending on the local y+ value.

Table 4 shows that the y+ values are well below 5, indicating that the near-wall region is appropriately resolved according to the rule of thumb. The table also shows that the drag coefficient approaches the expected value of 1.6 when the base cell size is 10 mm or smaller. Although y+ increases as the cell size decreases, all values remain far below 5. Therefore, the improved accuracy in the drag coefficient is likely due to better overall flow resolution around the model rather than improvements in the near-wall description.

Table 4. Simulation results for a two-dimensional rectangular box.

Base cell size [mm]	Number of cells	y+	CD
50	1,932	0.011	2.00
10	11,240	0.017	1.60
1	88,361	0.028	1.61
0.23	386,443	0.033	1.61

Figure 14 shows that although the drag coefficients for the three most refined mesh sizes are nearly identical in terms of mean value, their time histories differ noticeably. Because vortex shedding is expected for Re > 200, the drag coefficient should exhibit time-dependent behaviour, with the shedding characteristics influenced by the L/D ratio of the rectangular body, see Sohankar et al. (2021) for further details. Consequently, convergence cannot be evaluated solely on the basis of average drag values, the temporal variation of the drag coefficient must also be considered. As seen in Figure 14, the time variation for the 10 mm mesh is significantly smaller than for the 1 mm and 0.23 mm meshes. No further analysis is provided here, but the results clearly highlight the importance of reporting not only average values.

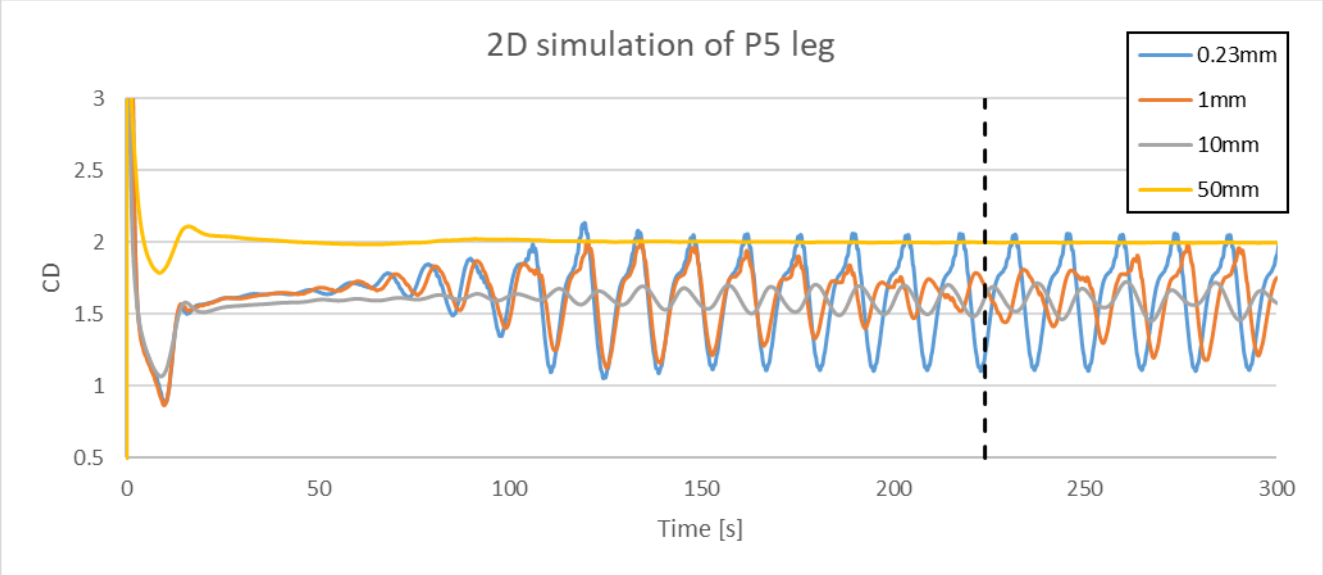

Fig. 14. Influence of base cell size on the drag coefficient for the rectangular object. The dashed line shows the time from when the averaged drag value is calculated.

5.2. THREE-DIMENSIONAL SIMULATION ON RECTANGULAR BOX

5.2.1. SET-UP OF SIMULATION IN STAR-CCM+

Simulations are carried out for a three-dimensional representation of the two-dimensional case presented in the previous chapter. Figure 15 shows a portion of the computational domain. In the earlier simulations, the z-direction was not resolved, but in the 3D model, the flow can also develop velocity components in this direction. Therefore, the z-extent of the domain must be sufficiently large to approximate two-dimensional behaviour. The chosen z-dimension is arbitrary, and the influence of the side walls has not been investigated.

The expected drag coefficient corresponds to the values shown in Figure 12. All simulations are performed using the transient model with the same numerical settings as previously applied.

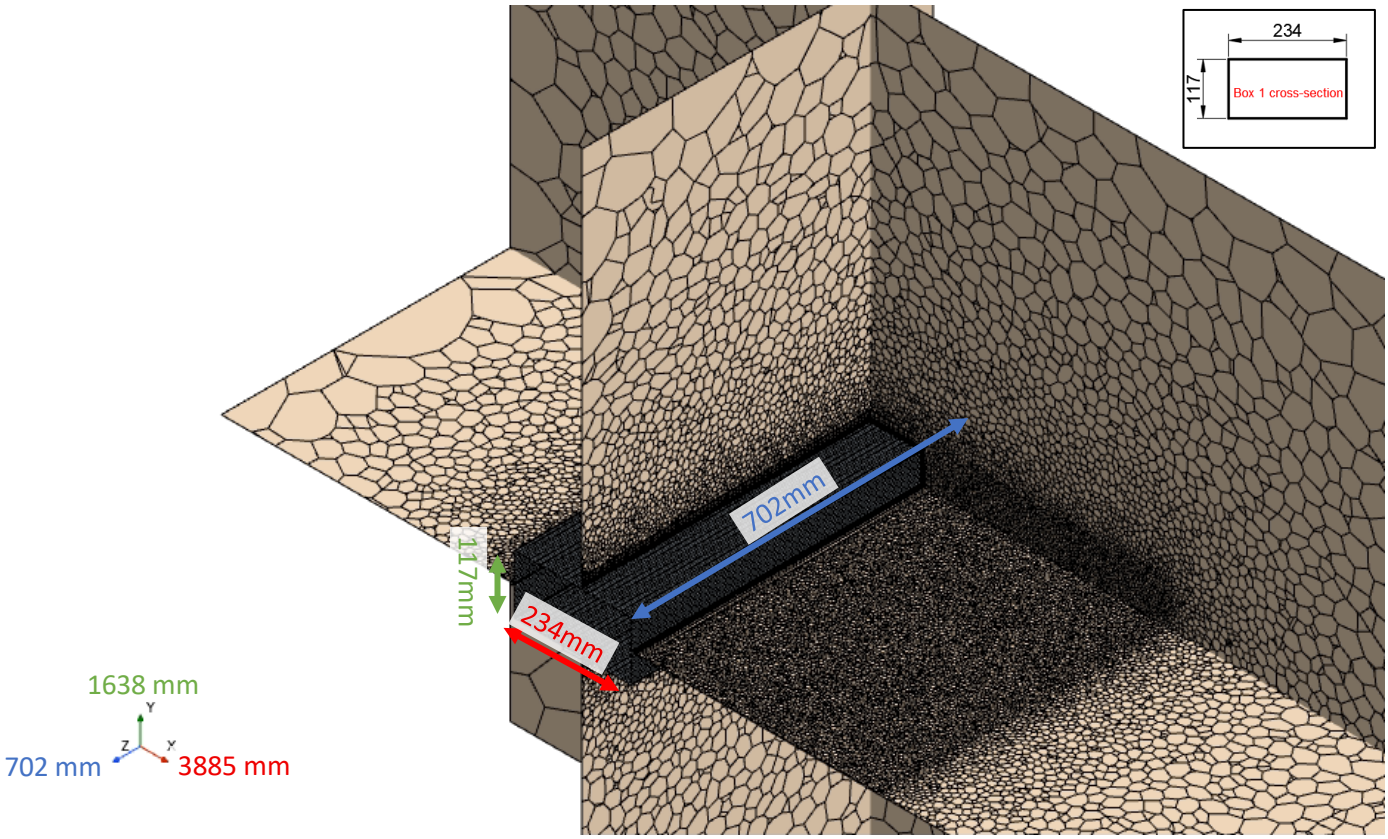

Fig. 15. Dimensions in the bottom left corner show the size of the domain, while the dimensions in the model domain show the dimensions of the rectangular shape.

5.2.2. RESULTS

Table 5 shows the results for the 2D and 3D simulations. It can be seen that the two simulations provide similar drag coefficients. It is noted that the number of cells increases significantly for the 3D model as the *z*-direction is now resolved.

Table 5. Simulation results for a three-dimensional rectangular box.

Model dimensions	Base cell size [mm]	Number of cells	CD
2D	10	11,240	1.60
3D	10	1,406,468	1.59

Figure 16 presents the time variation of the drag coefficient for the 2D and 3D simulations. The 2D simulation converges to a steady state more quickly than the 3D simulation. Once both have converged, the minimum and maximum values are nearly identical, though the time variations differ slightly.

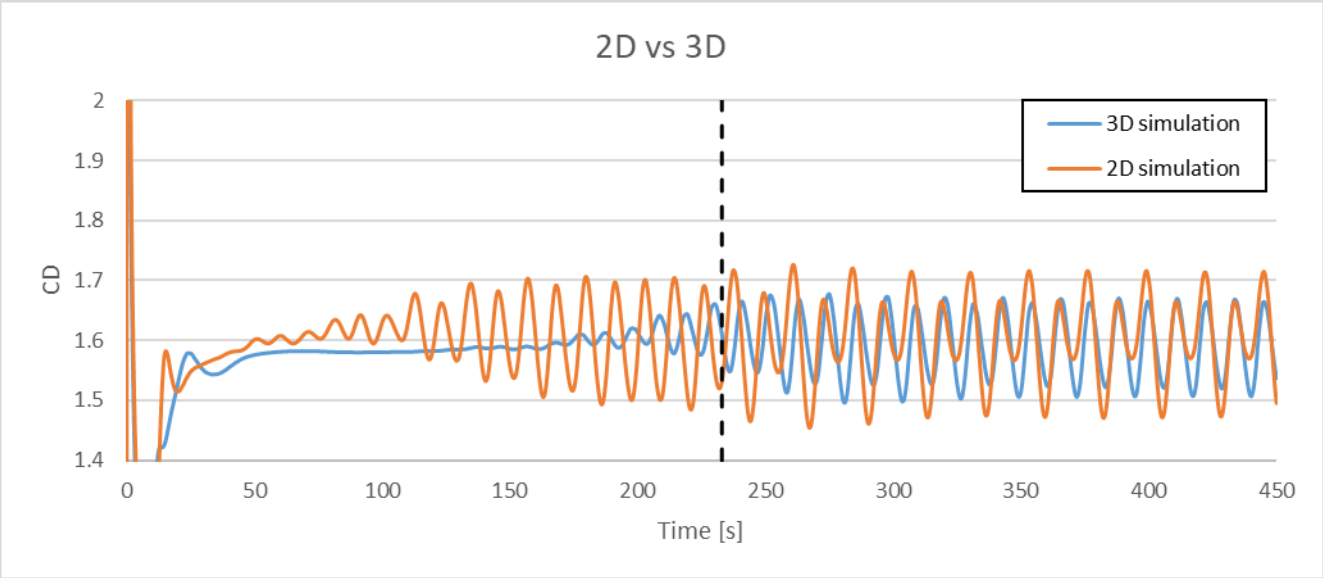

Fig. 16. Drag coefficient for two and three-dimensional simulations for the rectangular object. The dashed line shows the time from when the averaged drag value is calculated.

5.3. THREE-DIMENSIONAL P5 LEG FULLY SUBMERGED

The model configuration from the previous chapter has been adjusted so that the rectangular box does not span the entire length in the z-direction, as opposed to the previous case. This allows the flow to pass around the object on all sides.

5.3.1. SET-UP OF SIMULATION IN STAR-CCM+

The size in the *z*-direction of the object is reduced to 252 mm so that it fits with the submerged part of the P5 element used in the WindFlex model, as shown in Figure 17. It should be noted that the simulation is still only with a single phase, and therefore, it is not the full size of the P5 leg that is simulated, as some of it is above still water. The geometry and mesh of the model are shown in Figure 17.

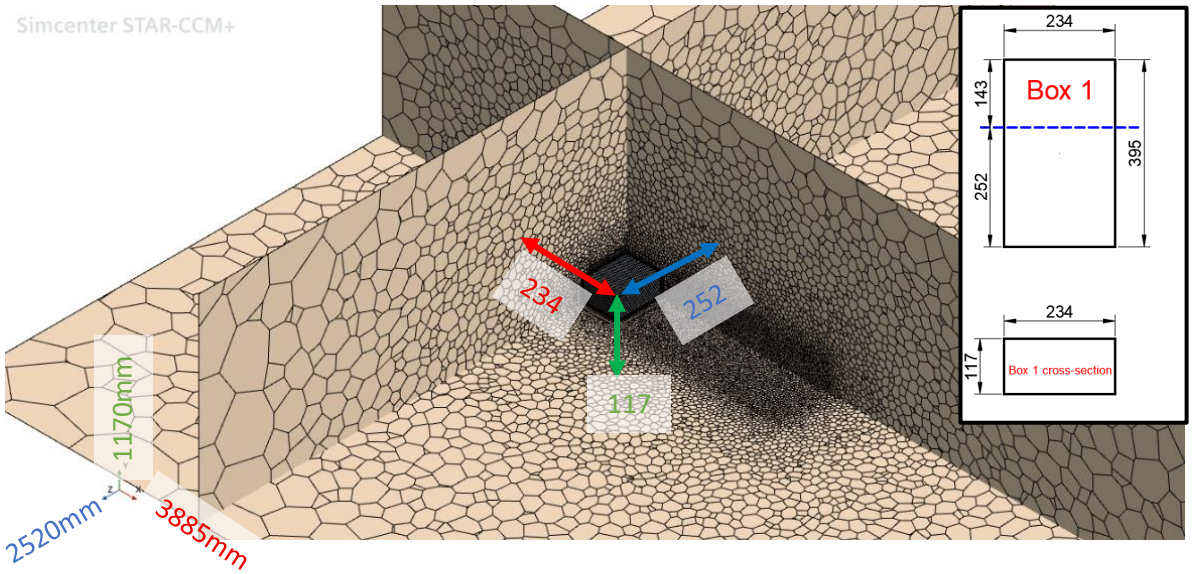

Fig. 17. Dimensions in the bottom left corner show the size of the domain, while the dimensions in the model domain show the dimensions of the rectangular shape.

5.3.2. RESULTS

No expected value for the drag could be found in the literature, but as the flow can now pass all sides of the object, the drag coefficient should be smaller than the one from the previous model, which gave ≈ 1.6. The results of the model are presented in Table 6. Here, the drag coefficient is 0.96. The time variation of the drag is shown in Figure 18 and it is observed that the drag coefficient becomes constant. The constant value results from the absence of vortex shedding behind the model, which is the opposite of what is expected. The reason for the vortex not being generated is most likely due to the mesh resolution not being fine enough, as also shown in Figure 14. No further studies on mesh resolution were conducted in this study.

Table 6. Simulation results for the P5 fully submerged.

Base cell size [mm]	Number of cells	Simulated time [s]	Wall clock [s]	Time ratio	C_D
10	761,531	450	29,909	66	0.96

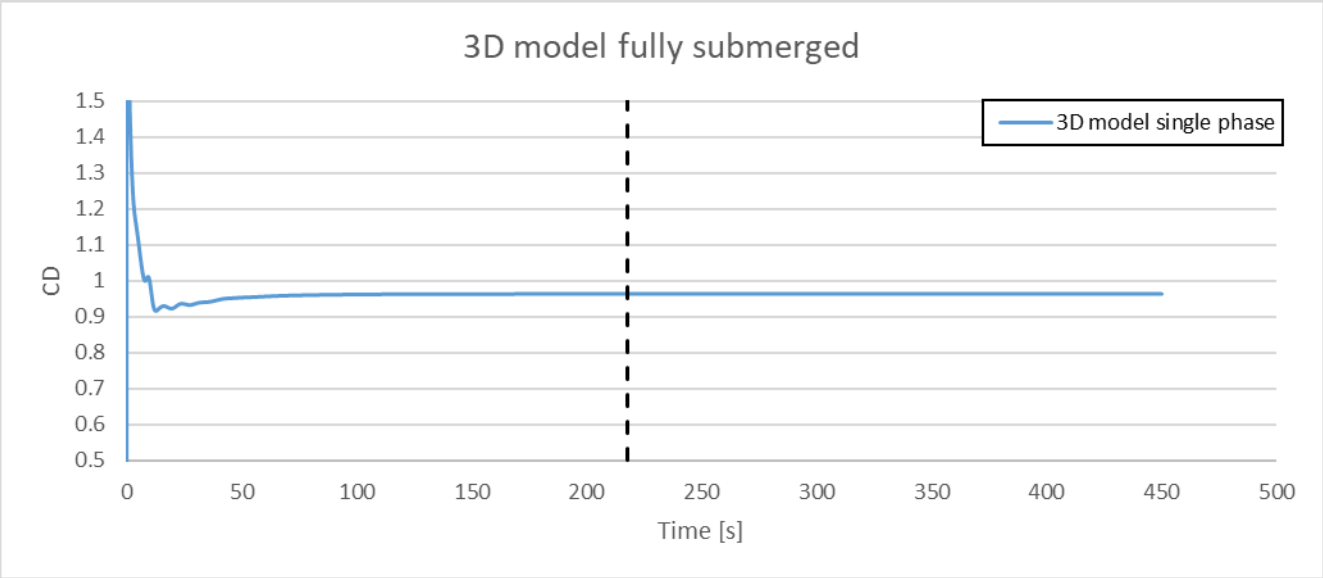

Fig. 18. Drag coefficient for three-dimensional simulations for the P5 leg.

5.4. THREE-DIMENSIONAL P5 LEG AT SYMMETRY BOUNDARY

The simulation has been modified to prevent flow from passing freely around the model, representing the condition in which the P5 leg intersects the water surface.

5.4.1. SET-UP OF SIMULATION IN STAR-CCM+

To prevent flow from passing along one side of the P5 leg, a symmetry boundary has been introduced on the side of the domain adjacent to the leg. The updated geometry and mesh are shown in Figure 19.

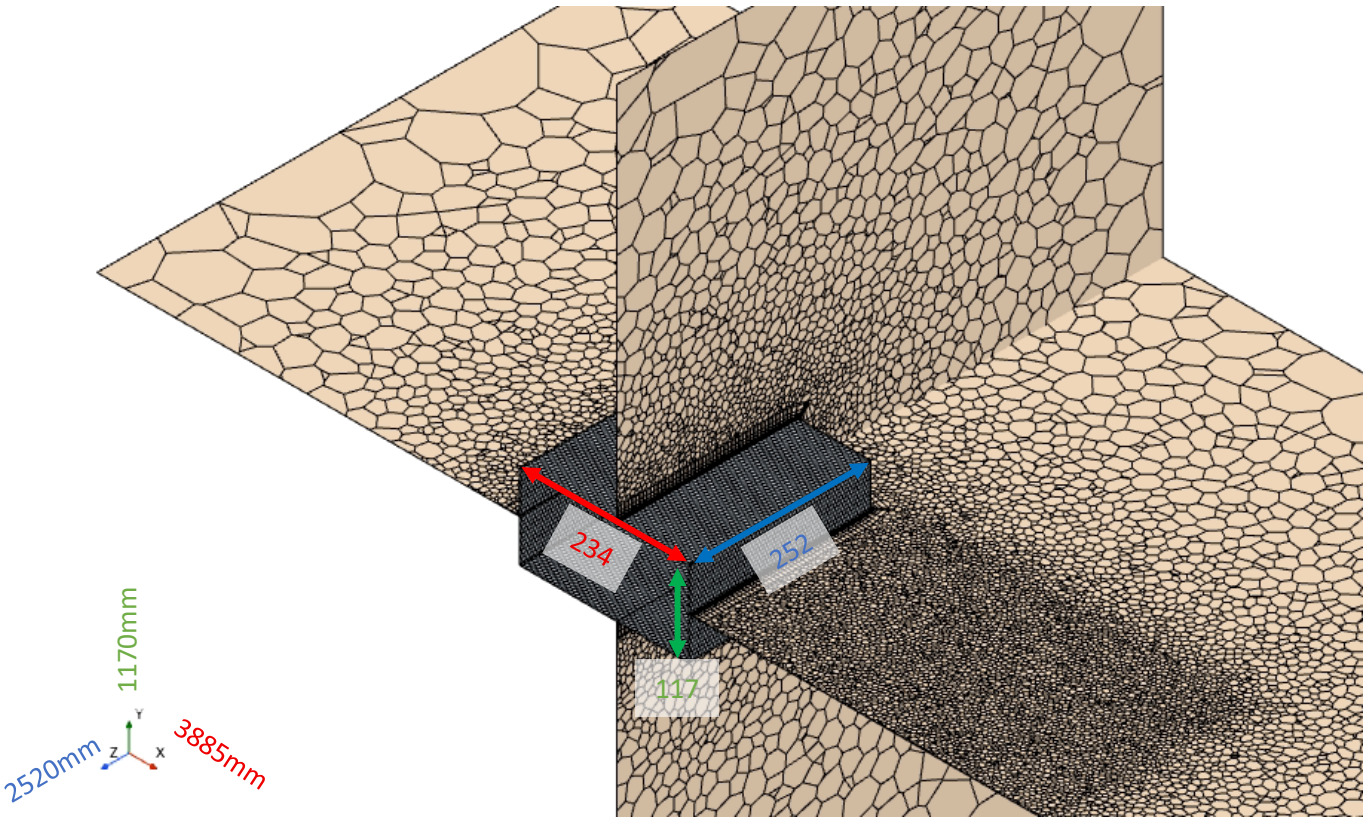

Fig. 19. Dimensions in the bottom left corner show the size of the domain, while the dimensions in the model domain show the dimensions of the rectangular shape.

The expected drag coefficient of the model can be found from Table 5-5 in RP-C205 by DNV (2025), which is valid for deck houses on a horizontal surface, see Figure 20. The drag coefficient depends on the side lengths, which are given in Table 7.

Table 7. Dimensions and side length ratios of the simulated object.

h [mm]	d [mm]	b [mm]	b/d [-]	h/b [-]
252	234	117	0.5	2.15

From Figure 20 and the side length ratios in Table 7, then the expected drag coefficient is 0.8, as shown in the red box.

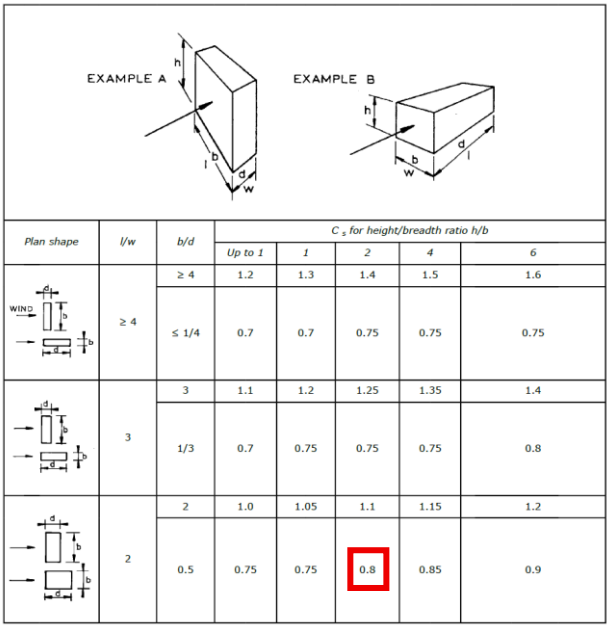

Plan shape	l/w	b/d	C_s for height/breadth ratio h/b				
			Up to 1	1	2	4	6
WIND	≥ 4	≥ 4	1.2	1.3	1.4	1.5	1.6
		≤ 1/4	0.7	0.7	0.75	0.75	0.75
	3	3	1.1	1.2	1.25	1.35	1.4
		1/3	0.7	0.75	0.75	0.75	0.8
	2	2	1.0	1.05	1.1	1.15	1.2
		0.5	0.75	0.75	0.8	0.85	0.9

Fig. 20. Drag coefficient on a rectangular shape, depending on the side length ratio from Table 5-5 in RP-C205 by DNV (2025).

5.4.2. Results

The simulation results are summarised in Table 8, showing a drag coefficient of 1.17, which is higher than the expected value of 0.8. Figure 18 illustrates the time history of the drag coefficient, which quickly reaches a constant value. This steadiness is likely due to the absence of vortex shedding behind the model, which may explain the deviation from the expected drag. Further studies could explore whether reducing the mesh size would induce vortex shedding and yield drag coefficients closer to the expected value.

Table 8. Simulation results for the P5 at symmetry plane.

Base cell size [mm]	Number of cells	Simulated time [s]	Wall clock [s]	Time ratio	CD
10	613,586	277	8375	30	1.17

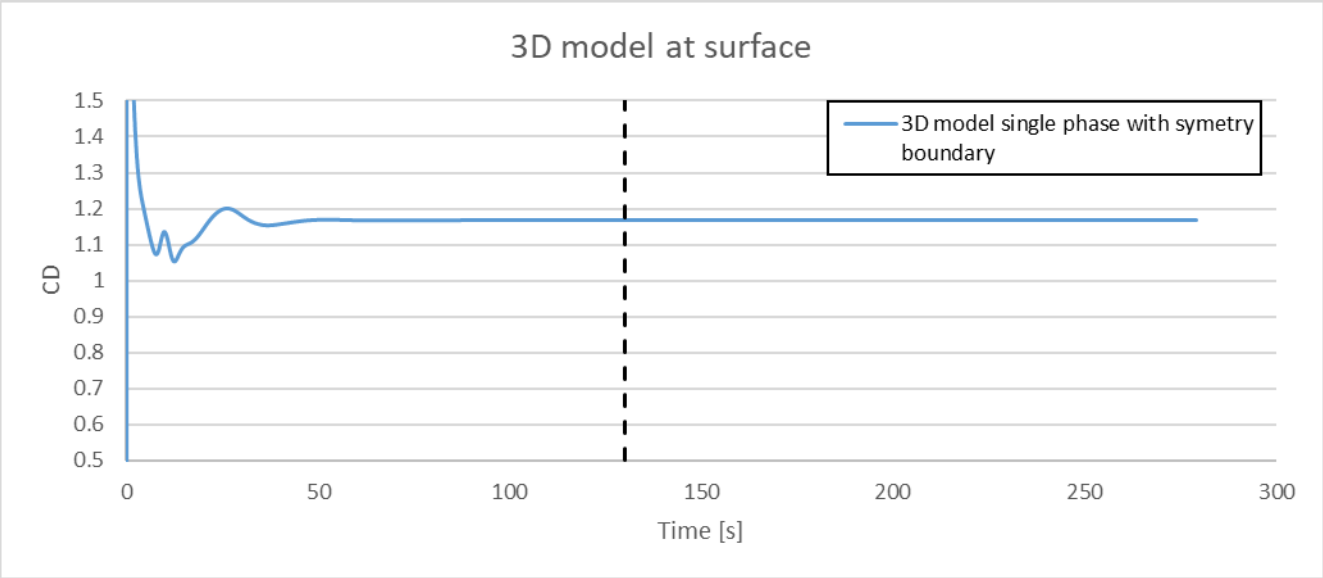

Fig. 21. Drag coefficient for three-dimensional simulations for the P5 leg.

6. Two-Phase Simulation with a Rectangular Box

6.1. Three-dimensional P5 leg at still water

Previous simulations have only been modelled with one phase, and now a model with two phases of fluid is made. The fluids are water and air, and the Volume of Fluid (VOF) approach is used to separate the two fluids.

6.1.1. Set-up of simulation in STAR-CCM+

The size of the new model domain is shown in Figure 22. The water level is set 1500 mm above the bottom of the domain, so that the domain consists of 50% water and 50% air. The density of water used is 998.2 kg/m^3, and for air, it is 1.18 kg/m^3. The used dynamic viscosity of water is 1 mPa·s, and for air, it is 0.0186 mPa·s. Gravity is now also included when dealing with multiple phases, and for the gravity, a value of 9.82 m/s^2 is applied.

The boundary conditions of the bottom and top of the domain are specified as *Velocity Inlet*. For the inlet and the sides of the domain, the boundary is specified as a *Velocity Inlet* with *VOF Wave Damping*. The velocity inlet has a constant velocity of 0.0707 m/s, and the wave damping has a distance of 0.1 m from the boundary into the domain. The wave-damping distance should be investigated further in future studies when actual waves are generated by the moving object. The damping can be used to restrict the vertical movement of the fluid. The outlet is specified as a *Pressure Outlet* with *VOF Wave Damping*. The pressure outlet specifies that there should be hydrostatic pressure on the boundary. The boundary for the object is set to a wall.

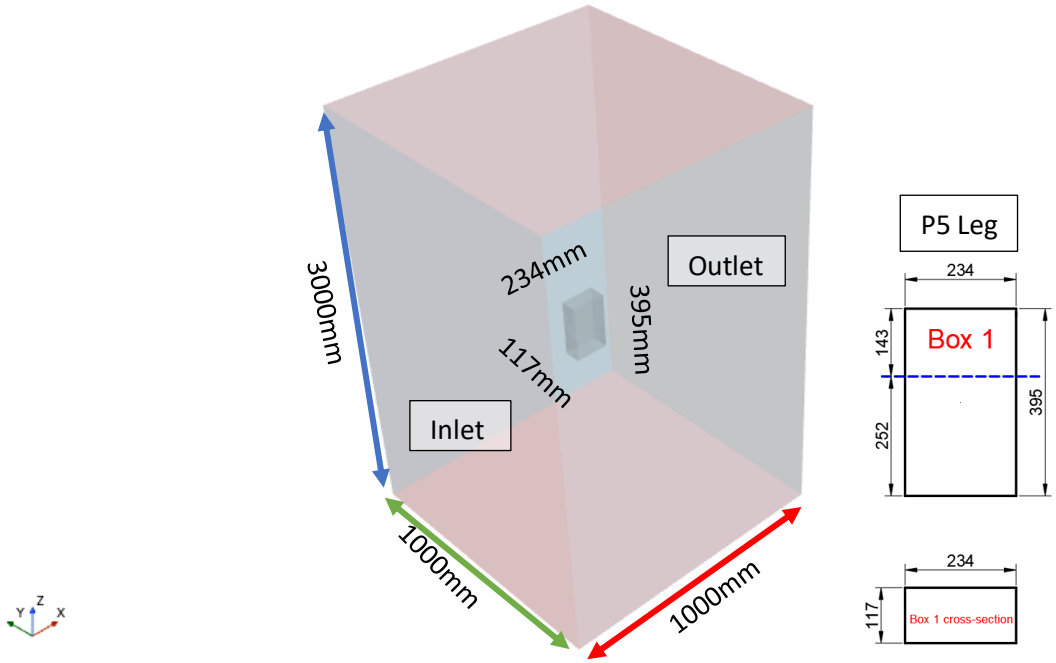

Fig. 22. Dimension of the model used in the VOF simulations.

The mesh is generated with the *Trimmed Cell Mesher* method. For the mesh generation, a *Base Size* of 1m is applied. The *Target Surface Size* and *Minimum Surface Size* of the mesh on the surfaces of the model

boundary are set to 1% of the *Base Size*. For the object, the *Target Surface Size* and *Minimum Surface Size* are set to 0.5%. From the object and outwards, 30 prism layers are used with a fixed size of 60mm.

The mesh is refined around the SWL with an anisotropic geometry. A finer resolution is applied ±100mm in the *z*-direction from the SWL with the mesh being 10% of the *Base Size* in the *x*- and *y*-direction and 2.5% in the *z*-direction. A coarser refinement is applied ±200mm from SWL with 20% in the *x*- and *y*-direction and 5% in the *z*-direction. A wake refinement with a base size of 2.5% of the *Base Size* is also made downstream of the object. The mesh can be seen in Figure 23.

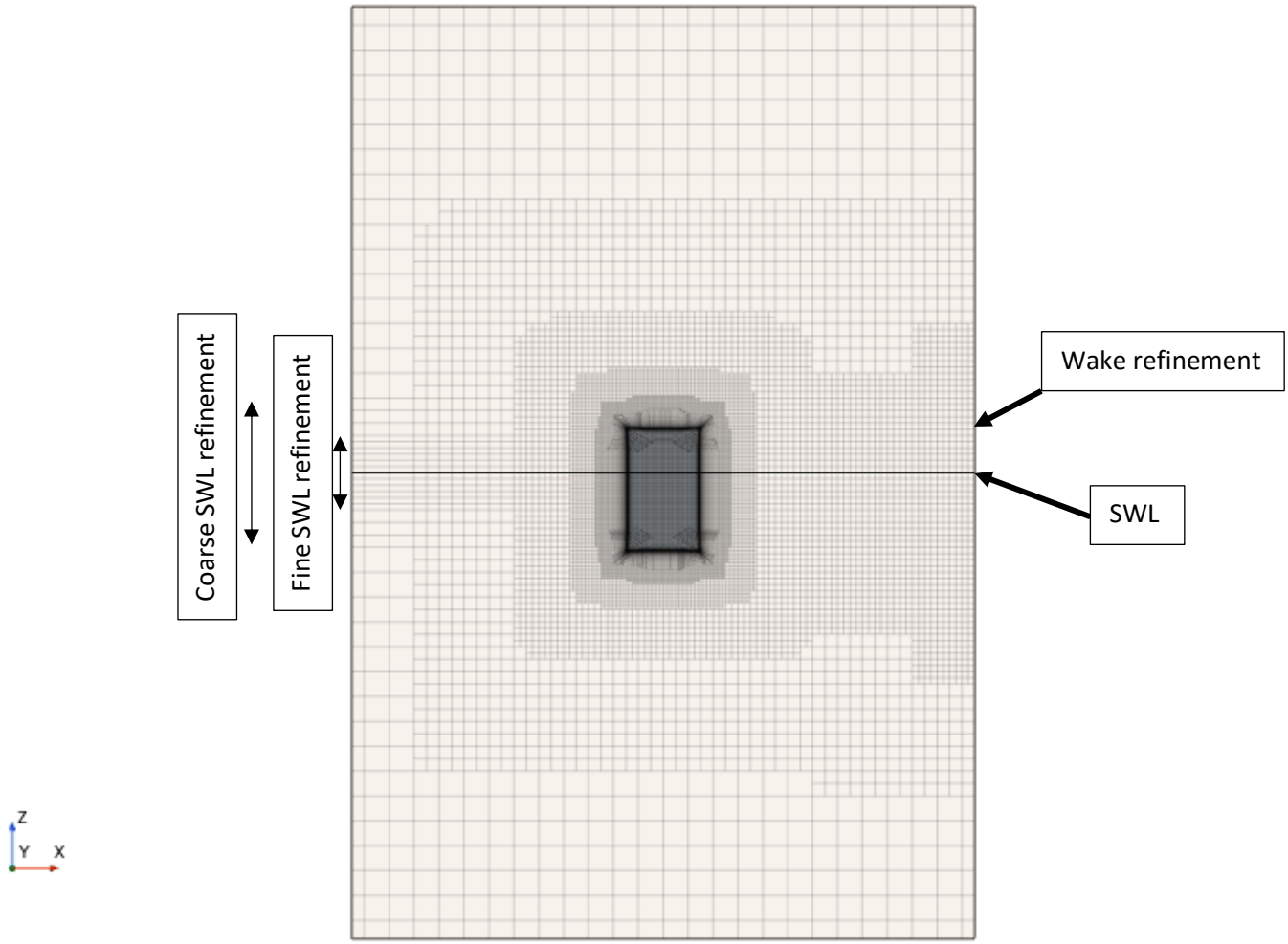

Fig. 23. Side view of mesh with a base size of 1m.

The model was created as a transient simulation. The time step is controlled by the Courant-Friedrichs-Lewy (CFL) number, which is set to 0.5. A K-epsilon turbulence model is applied.

6.1.2. Results

The model results are summarized in Table 9. The drag coefficient is found to be 1.09, slightly lower than the simulated value reported in the previous chapter (CD = 1.17). However, this simulated drag coefficient aligns more closely with the value shown in Figure 20, even though that case considered an object positioned on top of a fixed surface, whereas here the surface is modelled as a free water surface. Figure 24 presents the

time evolution of the drag, showing that the drag coefficient varies initially and stabilizes after approximately 30 seconds. Although the drag coefficient is expected to oscillate due to vortex shedding, this phenomenon does not appear in the simulation, likely due to the coarse mesh size. These results can serve as a baseline for future studies, which could focus on optimising the model to better match literature values before simulating a moving object.

Table 9. Model results for VOF simulation.

Base cell size [mm]	Number of cells	Simulated time [s]	Wall clock [s]	Time ratio	CD
1000	1,367,314	60	226,677	3,778	1.09

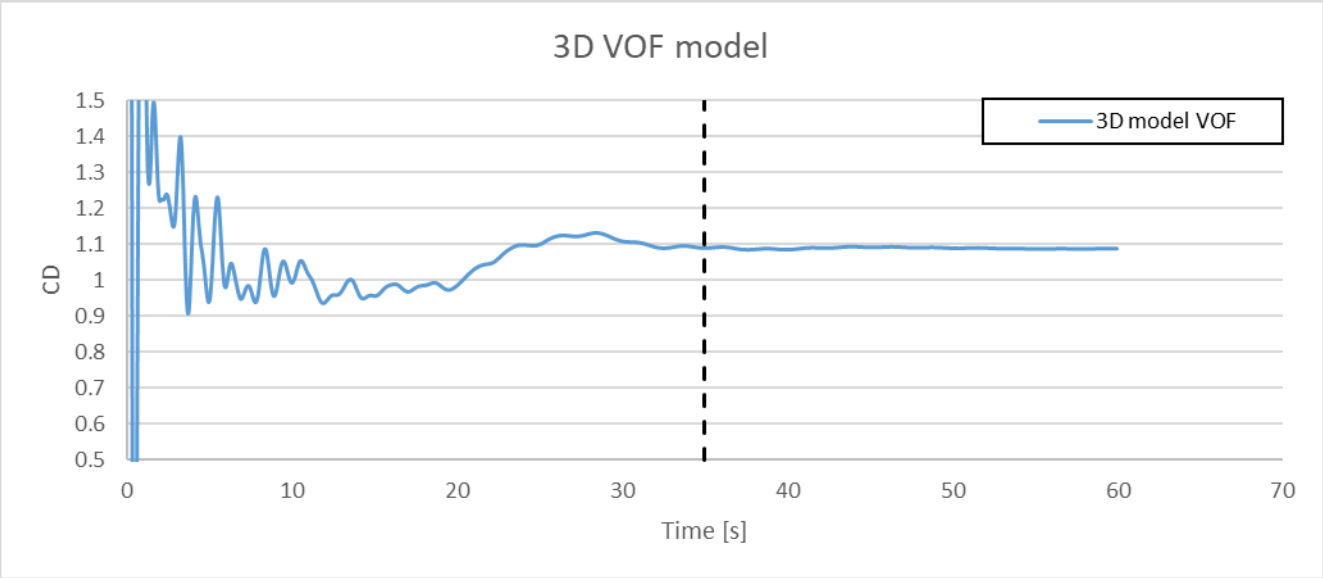

Fig. 24. Drag coefficient for VOF simulation. The black dashed line illustrates the time from when the average value is taken.

7. CONCLUSIONS

The present report has analysed the drag behaviour of simplified and project-specific geometries using Computational Fluid Dynamics (CFD) in STAR-CCM+. Validation against well-documented cases, including two-dimensional simulations of squares and rectangles, demonstrated that the numerical model can reproduce drag coefficients in reasonable agreement with reference data from DNV (2025), Yen and Yang (2011), and Blevins (1984).

The results showed that transient simulations generally provide more realistic drag coefficients compared to steady-state solutions, particularly when flow separation and vortex shedding occur. For the rectangular and P5 leg geometries, both two- and three-dimensional simulations indicated convergence toward expected values, though deviations were observed in cases where vortex shedding was not adequately captured, most likely due to mesh resolution limitations.

Introducing symmetry boundaries and free-surface effects further highlighted the sensitivity of the drag predictions to boundary conditions and modelling approaches. The Volume of Fluid (VOF) simulations produced drag coefficients closer to expected reference values, suggesting that multi-phase modelling improves the physical realism of the results.

Overall, the study confirms that STAR-CCM+ can be applied to estimate hydrodynamic loads on box-type elements with reasonable accuracy, provided that sufficient attention is given to mesh refinement, turbulence modelling, and appropriate transient setups.

8. FUTURE WORK

The findings of this work lay the groundwork for the next phase of the project, which will focus on simulations involving moving structures. The first step will be to compare numerical simulations directly with existing experimental data to evaluate model performance and identify aspects needing refinement. These comparisons will serve as an essential validation step before progressing to more complex configurations.

The next study may examine drag coefficients on WindFlex platform components subjected to prescribed dynamic motions in calm water, providing insight into drag behaviour and wave radiation effects. This work can then be extended to include excitation forces and the combined influence of structural motion and incident waves, moving toward a more complete hydrodynamic representation.

Ultimately, the future work aims to bridge the gap between the present studies and the developments documented in Eskilsson and Kramer (2025), establishing a foundation for further model development that will enable calculations for varying platform geometries.

9.REFERENCES

A., M., Sohankar, A., Alam, M., & Md. (2021). Flow over rectangular cylinder: Effects of cylinder aspect ratio and Reynolds number. *International Journal of Mechanical Sciences, 195*.

Blevins, R. D. (1984). *Applied fluid dynamics handbook.* New York.

DNV. (2025). *Environmental Conditions and Environmental Loads: Recommended Practice DNV-RP-C205.*

Eskilsson, C., & Kramer, M. B. (2025). *CFD Simulations of the Floating Power Plant WindFlex Platform.* Department of the Built Environment. Aalborg University. ISSN 1901-726X, DCE Technical Report No. 330.

HydroFlex. (2025a). *Description of Models for the HydroFlex Components Phase 1 Tests. HydroFlex internal project report with document no. 801-FPP-0151, Rev 1, 2025-03-10.*

HydroFlex. (2025b). *Target Motion in PTS22-24. HydroFlex internal project report No. 801-FPP-0138, Rev4.*

HydroFlex. (2025c). *AAU WindFlex Mark2 - Description of Model. HydroFlex internal project report No. 801-FPP-0133, Rev4.*

Yen, S. C., & Yang, C. W. (2011). Flow patterns and vortex shedding behavior behind a square cylinder. *Journal of Wind Engineering and Industrial Aerodynamics, 99*(8), 868-878.